Growth of single-crystal CrN on MgO(001): Effects of low-energy ion-irradiation on surface morphological evolution and physical properties

D. Gall, C.-S. Shin, and T. Spila
Department of Materials Science and Frederick Seitz Materials Research Laboratory, University of Illinois, 1101 West Springfield Avenue, Urbana, Illinois 61801

M. Odén
Department of Mechanical Engineering, Linköping University, S-581 83 Linköping, Sweden

M. J. H. Senna, J. E. Greene, and I. Petrov
Department of Materials Science and Frederick Seitz Materials Research Laboratory, University of Illinois, 1101 West Springfield Avenue, Urbana, Illinois 61801

(Received 24 September 2001; accepted for publication 30 November 2001)

CrN layers, 0.5 μm thick, were grown on MgO(001) at $T_s = 570-775\,^{\circ}\mathrm{C}$ by ultrahigh vacuum magnetically unbalanced magnetron sputter deposition in pure N_2 discharges at 20 mTorr. Layers grown at $T_s \leqslant 700\,^{\circ}\mathrm{C}$ are stoichiometric single crystals exhibiting cube-on-cube epitaxy: $(001)_{\mathrm{CrN}}||(001)_{\mathrm{MgO}}$ with $[100]_{\mathrm{CrN}}||[100]_{\mathrm{MgO}}$. At higher temperatures, N_2 desorption during deposition results in understoichiometric polycrystalline films with N fractions decreasing to 0.35, 0.28, and 0.07 with $T_s = 730$, 760, and 775 °C, respectively. The surface morphologies of epitaxial CrN(001) layers were found to depend strongly on the incident ion-to-metal flux ratio $J_{N_2^+}/J_{\mathrm{Cr}}$ which was varied between 1.7 and 14 with the ion energy maintained constant at 12 eV. The surfaces of layers grown with $J_{N_2^+}/J_{\mathrm{Cr}} = 1.7$ consist of self-organized square-shaped mounds, due to kinetic roughening, with edges aligned along orthogonal ⟨100⟩ directions. The mounds have an average peak-to-valley height $\langle h \rangle = 5.1$ nm and an in-plane correlation length of $\langle d \rangle = 0.21$ μm. The combination of atomic shadowing by the mounds with low adatom mobility results in the formation of nanopipes extending along the growth direction. Increasing $J_{N_2^+}/J_{\mathrm{Cr}}$ to 14 leads, due to increased adatom mobilities, to much smoother surfaces with $\langle h \rangle = 2.5$ nm and $\langle d \rangle = 0.52$ μm. Correspondingly, the nanopipe density decreases from 870 to 270 $\mu\mathrm{m}^{-2}$ to <20 $\mu\mathrm{m}^{-2}$ as $J_{N_2^+}/J_{\mathrm{Cr}}$ is increased from 1.7 to 6 to 10. The hardness of dense CrN(001) is 28.5 ± 1 GPa, but decreases to 22.5 ± 1 GPa for layers containing significant nanopipe densities. The CrN(001) elastic modulus, 405 ± 15 GPa, room-temperature resistivity, 7.7×10^{-2} Ω cm, and relaxed lattice constant, 0.4162 ± 0.0008 nm, are independent of $J_{N_2^+}/J_{\mathrm{Cr}}$. © *2002 American Institute of Physics.*

[DOI: 10.1063/1.1446239]

I. INTRODUCTION

Transition-metal (TM) nitrides are well known for their remarkable physical properties including high hardness and mechanical strength, chemical inertness, and high-temperature stability. As a result, they are widely studied and have become technologically important for applications such as hard wear-resistant coatings, diffusion barriers, and optical coatings. CrN has gained considerable interest over the past several years due to its superior high-temperature oxidation resistance,[1–3] considerably higher than that of TiN, the primary industrial TM-nitride hard coating. CrN has also been shown to possess high wear[4,5] and corrosion resistance,[6] to provide improved system adherence as an interfacial layer between diamond films and steel,[7] and to offer potential for use in phase-shift masks for photolithography[8] and etch-resistant hardmasks for x-ray absorber patterning.[9]

Reported physical properties of polycrystalline CrN_x layers, typically deposited by reactive sputtering or arc evaporation, vary dramatically with growth parameters.[10–14] Resistivities, for example, range over more than six orders of magnitude from 3×10^2 to 6×10^8 $\mu\Omega$ cm[15–18] and hardness values for CrN_x vary from 13 to 31 GPa.[4,10,11,19–21] While these large differences are presumably due to corresponding differences in the composition and microstructure of the polycrystalline CrN_x films, the layers are generally poorly characterized. Moreover, data interpretation is also hampered by the fact that the fundamental properties of single-crystal CrN are unknown. Finally, CrN_x, like other TM nitrides, exhibits wide single-phase fields. x ranges from 0.4 to 0.7 in the hexagonal β-Cr_2N phase and from 0.8 to 1.0 for the cubic-$B1$ NaCl structure.[22]

As an initial step in determining the fundamental properties of NaCl- structure CrN, we have grown epitaxial stoichiometric CrN layers on MgO(001), characterized film microstructure as a function of growth temperature and incident ion flux, and measured the relaxed lattice constant, hardness, elastic modulus, and room-temperature resistivity. The layers were grown by ultrahigh vacuum (UHV) magnetically unbalanced reactive magnetron sputtering in pure N_2 at 20 m Torr and temperatures T_s between 570 and 775 °C. Layers

grown at $T_s \leq 700\,^{\circ}\mathrm{C}$ were found to be epitaxial stoichiometric (N/Cr = 1) NaCl-structure CrN(001) while growth at higher temperatures leads to understoichiometric multiphase polycrystalline films consisting of NaCl-structure CrN_x, hexagonal β-Cr_2N, and bcc-Cr grains. We chose $T_s = 600\,^{\circ}\mathrm{C}$ to investigate the effect of low-energy N_2^+ ion irradiation during growth on the microstructural evolution and physical properties of epitaxial CrN(001) layers. The incident N_2^+/Cr flux ratio $J_{N_2^+}/J_{Cr}$ was varied from 1.7 to 14 while maintaining the N_2^+ ion energy $E_i = 12$ eV, well below the threshold energy for bulk lattice-atom displacement.[23] We find that the use of high-flux, low-energy ion irradiation during CrN(001) growth is crucial for obtaining dense layers with smooth surfaces.

The hardness H of fully dense epitaxial stoichiometric CrN(001) is 28.5 ± 1 GPa, while H decreases to 22.5 ± 1 GPa in underdense layers. The CrN(001) elastic modulus, 405 ± 15 GPa, room-temperature resistivity, $7.7 \times 10^{-2}\ \Omega\,\mathrm{cm}$, and relaxed lattice constant, 0.4162 ± 0.0008 nm, are independent of $J_{N_2^+}/J_{Cr}$.

II. EXPERIMENTAL PROCEDURE

All CrN_x layers were grown in a load-locked multichamber UHV stainless-steel dc magnetron sputter deposition system described in detail in Ref. 24. The pressure in the sample introduction chamber was reduced to less than 5×10^{-8} Torr (7×10^{-6} Pa), using a $50\,\mathrm{l\,s^{-1}}$ turbomolecular pump (TMP), prior to initiating substrate exchange into the deposition chamber which has a base pressure of 5×10^{-10} Torr (7×10^{-8} Pa), achieved using a $500\,\mathrm{l\,s^{-1}}$ TMP. A water-cooled 6.35-cm-diam Cr target with a purity of 99.99% was mounted 10 cm from the substrate holder. Sputtering was carried out at a constant power of 150 W in pure N_2 (99.999%), introduced through a high precision solenoid valve, at 20 mTorr (2.67 Pa). The pressure was measured by a capacitance manometer and maintained constant with an automatic mass-flow controller. The deposition rate was 0.4 $\mathrm{nm\,s^{-1}}$.

A pair of external Helmholtz coils with Fe pole pieces were utilized to create a uniform axial magnetic field, $0 \leq B_{ext} \leq 180$ G, in the region between the target and the substrate in order to shape the discharge and provide independent control of the ion flux incident at the growing film with negligible effect on the target atom flux.[24]

The substrates were polished $10 \times 10 \times 0.5\ \mathrm{mm^3}$ MgO(001) wafers cleaned with successive rinses in ultrasonic baths of trichloroethane, acetone, methanol, and deionized water and blown dry with dry N_2. The wafers were then mounted on resistively heated Ta platens using Mo clips and inserted into the sample introduction chamber for transport to the growth chamber where they were thermally degassed at 800 °C for 1 h, a procedure shown to result in sharp MgO(001)1×1 reflection high-energy electron-diffraction patterns.[25] Just prior to initiating deposition, the target was sputter etched for 5 min with a shutter shielding the substrate. The film growth temperature, $570 \leq T_s \leq 775\,^{\circ}\mathrm{C}$ including the contribution due to plasma heating, was measured with a pyrometer calibrated by a thermocouple bonded to a CrN-coated MgO substrate. Following deposition, the samples were allowed to cool to $< 100\,^{\circ}\mathrm{C}$ before transferring them to the load lock chamber which was then vented with dry N_2.

Plasma characteristics in the vicinity of the substrate during film growth were determined from probe measurements following the procedures described in Ref. 24. The current-measuring probe was a 6-mm-diam CrN-coated stainless-steel disk mounted in a through hole drilled in the center of a special substrate platten. The probe was situated such that its surface was in the plane of the substrate and it was electrically isolated from the platten by a 0.25 mm vacuum gap. To minimize edge effects, the probe and substrate holder were maintained at the same potential with respect to the anode.

CrN layer compositions, i.e., N/Cr ratios, were determined by Rutherford backscattering spectroscopy (RBS). The probe beam consisted of 2 MeV He^+ ions incident at an angle of 22.5° relative to the sample surface normal with the detector set at a 150° scattering angle. Backscattered spectra were analyzed using the RUMP simulation program.[26] The uncertainty in reported N/Cr ratios is less than ± 0.03.

Film microstructure and texture were investigated using a combination of x-ray diffraction (XRD), plan-view transmission electron microscopy (TEM), and cross-sectional TEM (XTEM). The XRD measurements were carried out in a powder diffractometer system with a Cu K_α source and slit divergencies of 1° and 0.02° for ω-2θ scans and ω-rocking curves, respectively. The resulting resolution was 0.01° 2θ and 0.02° ω. Layer strain states were determined from high-resolution reciprocal lattice maps (HR-RLMs) around asymmetric 113 reflections using a Philips XPert diffraction system with a Cu $K_{\alpha 1}$ source.

TEM and XTEM analyses were performed in a Philips CM12 microscope with a LaB_6 filament at 120 kV. Plan-view specimens were prepared by mechanically thinning from the back side with SiC to a specimen thickness of $\simeq 30$ μm. Final thinning to electron transparency was accomplished by ion milling using a 5.0 kV Ar^+-ion beam incident at 12°. Cross-sectional specimens were prepared by gluing two samples film-to-film and then cutting vertical sections which were ground and milled in a manner similar to that of the plan-view samples, but from both sides.

Film surface morphology was investigated using contact-mode atomic force microscopy (AFM). AFM analyses were carried out in air using a Digital Instruments Multimode microscope with oxide-sharpened Si_3N_4 tips having radii of 5–40 nm. The images were linearly planarized to remove sample tilt effects during the measurements. Additional line-by-line leveling was performed to remove low-frequency vibrational noise. Height-difference, $G(\rho) = \langle |h_j - h_i|^2 \rangle$, and height-height, $H(\rho) = \langle h_i h_j \rangle$, correlation functions — where h_i and h_j are surface heights at positions i and j separated by a distance ρ and the brackets correspond to averages over the measured surface — were calculated from the AFM images. Values for the dominant in-plane length scale $\langle d \rangle$ were determined from the first maximum in $H(\rho)$. The surface width $\langle w \rangle$, which is equivalent to the root-mean-squared (rms) roughness, was obtained

using the relation $2\langle w^2\rangle = G(\rho) + 2H(\rho)$, and values for average peak-to-valley mound heights $\langle h\rangle$ were calculated from the surface widths, $\langle h\rangle = 2\sqrt{2}\langle w\rangle$.

Room-temperature resistivity was measured with spring loaded tips in a linear four-point probe geometry. The hardness and elastic modulus of CrN(001) layers were determined from nanoindentation responses measured using a Nano Indentor II instrument operated with a triangular Berkovich diamond tip that was calibrated following the procedure described in Ref. 27. Measurement sequences comprised of loading to maximum loads of 2, 4, 6, 8, 10, and 40 mN, holding for 10 s, and then unloading. A minimum of 25 indents was performed at each sequence. The hardness was determined from the unloading segments using the technique developed by Pharr and Oliver.[27] A more detailed description of the experimental procedure for hardness determination is presented in Ref. 28.

III. RESULTS AND DISCUSSION

A. Plasma characterization

Plasma characterization experiments show that the ion current density incident at the substrate during deposition increases from 0.6 to 2.3, 3.7, and 4.9 mA cm^{-2} with applied external magnetic fields B_{ext} of 0, 60, 120, and 180 G, respectively. This corresponds to ion fluxes ranging from 3.7×10^{15} to 3.1×10^{16} $s^{-1}\,cm^{-2}$ with $0\leqslant B_{ext}\leqslant 180$ G. Based upon energy- and mass-resolved analyses of ions incident at the substrate during reactive magnetron sputtering of Ti in pure N_2 discharges,[29] the dominant (>96%) ion species is N_2^+. Combining the measured ion flux with the deposition rate of 0.4 nm s^{-1}, which is found to be independent of B_{ext}, we obtain incident N_2^+/Cr flux ratios $J_{N_2^+}/J_{Cr}$ of 1.7, 6, 10, and 14 with $B_{ext}=0$, 60, 120, and 180 G. High ion-to-neutral ratios ($\geqslant 5$) have previously been shown to have a major effect on the microstructure of polycrystalline and epitaxial TiN,[30] ScN,[31] and $Ti_{1-x}Al_xN$[32] layers.

The vast majority of the ions incident at the substrate and growing film during deposition experienced the full sheath potential since the mean-free path for charge-exchange collisions, $\simeq 2$ mm,[33] was approximately a factor of 10 larger than the sheath width, $0.09\leqslant w_s\leqslant 0.27$ mm, estimated from the Child–Langmuir equation[34] using the measured current density, $0.6\leqslant j_i\leqslant 4.9$ mA cm^{-2} and the difference between the plasma and substrate potentials, $(V_p - V_s)\simeq 12$ V. The 12 eV N_2^+ ion energy is larger than the N_2 molecular binding energy of 9.7 eV[35] leading to N_2^+ dissociation upon collision with the film surface.

B. CrN_x composition vs T_s

The compositions of all CrN_x layers were determined by RBS. Spectra were obtained after tilting the substrate 37.5° away from the detector in order to increase the He^+ path through the CrN_x layer and shift the Mg substrate peak to lower energies in order to reduce the background signal under the N peak. Figure 1(a) is a typical RBS spectrum from a 0.5-μm-thick CrN/MgO(001) layer grown at 620 °C with $J_{N_2^+}/J_{Cr}=1.7$. The trapezoidal peak between 0.93 and 1.50 MeV is due to backscattering from Cr atoms. The onset of the N signal occurs at 0.67 MeV and the high intensity below 0.57 MeV is due to Mg atoms from the substrate. The solid line in Fig. 1(a) is the best fit through the data using the RUMP simulation program.[26] The area densities of Cr and N atoms are found to be identical, 2.61×10^{18} cm^{-2}. The CrN(001) layer is thus stoichiometric with a N/Cr ratio of 1.00 ± 0.03. The film thickness, 470 nm, determined using the RUMP simulation results together with the relaxed CrN lattice constant, $a_0=0.4162$ nm (see Sec. III C below), is in good agreement with the value obtained from deposition rate calibrations.

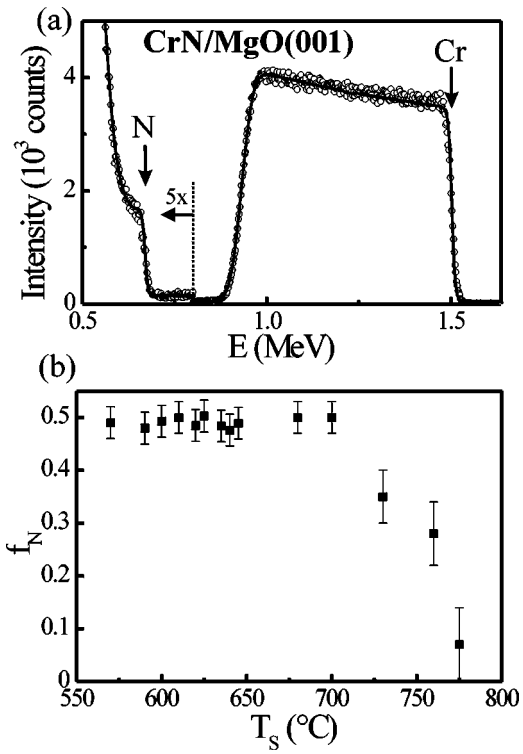

FIG. 1. (a) A typical RBS spectrum from an epitaxial 500-nm-thick CrN/MgO(001) layer grown at $T_s=620$ °C with $J_{N_2^+}/J_{Cr}=1.7$. (b) N atom fraction f_N in CrN layers grown as a function of T_s.

Figure 1(b) is a plot of measured N fractions f_N for a series of CrN_x(001) layers deposited as a function of T_s(550–775 °C) with $J_{N_2^+}/J_{Cr}=1.7$. The composition remains stoichiometric, $f_N=0.50\pm0.03$, for all layers grown at $T_s\leqslant 700$ °C. At higher deposition temperatures, f_N drops rapidly to 0.35, 0.28, and 0.07 with $T_s=730$, 760, and 775 °C. The stoichiometric layers are, as discussed below, NaCl-structure single crystals. However, as indicated by XRD and TEM analyses, the N-deficient layers are polycrystalline and multiphase, composed of NaCl-structure CrN_x, hexagonal β-Cr_2N, and N-doped bcc-Cr grains. The layer grown at 775 °C also contains some bcc-Cr grains, which grow with a 45°-rotated local epitaxial relationship to the MgO(001) substrate, $(001)_{Cr}||(001)_{MgO}$ with $[100]_{Cr}||[110]_{MgO}$. The 45° rotation occurs in order to reduce the local lattice constant mismatch, similar to previous reports for the epitaxial growth of W(001) on MgO(001).[36]

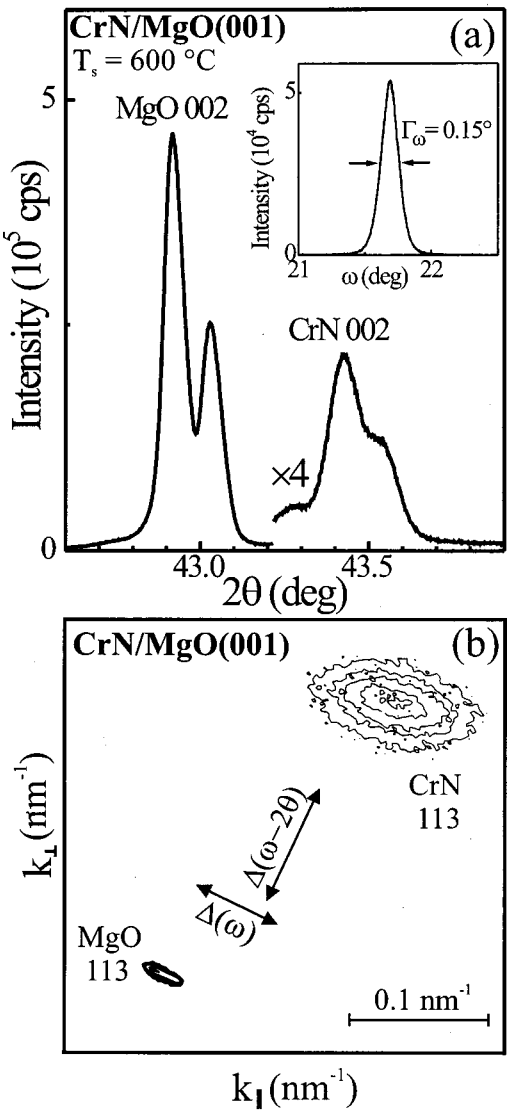

FIG. 2. X-ray diffraction (a) ω-2θ scan and (b) 113 HR-RLM from 500-nm-thick epitaxial CrN/MgO(001) layers grown at $T_s=600\,^{\circ}\mathrm{C}$ with $J_{N_2^+}/J_{Cr}=6$ and 1.7, respectively. The inset in (a) shows an ω-rocking curve from the 002 CrN peak.

The nitrogen loss at $T_s>700\,^{\circ}\mathrm{C}$ is due to an increasing rate of N_2 desorption from the growing films. In the following, we concentrate on growth and properties of NaCl-structure CrN(001) layers, that is, on layers grown at $T_s \leqslant 700\,^{\circ}\mathrm{C}$.

C. Microstructure and surface morphology

X-ray diffraction analyses show that all stoichiometric CrN(001) layers are single phase with the NaCl structure. The only CrN XRD peaks observed over the 2θ range between 20° and 80° are 002, irrespective of the incident flux ratio ($1.7 \leqslant J_{N_2^+}/J_{Cr} \leqslant 14$) and growth temperature ($570 \leqslant T_s \leqslant 700\,^{\circ}\mathrm{C}$). A narrow region of a typical XRD spectrum is shown in Fig. 2(a) for a CrN(001) layer grown at $T_s=600\,^{\circ}\mathrm{C}$ with $J_{N_2^+}/J_{Cr}=6$. The features at 42.91° and 43.02° are MgO 002 Cu $K_{\alpha 1}$ and $K_{\alpha 2}$ peaks ($a_{MgO}=0.4213$ nm), while the corresponding CrN peaks are centered at 43.42° and 43.54°, yielding a lattice constant $a_\perp$ along the film growth direction of 0.4165 nm. The full width at half maximum intensity $\Gamma_{2\theta}$ of the CrN 002 $K_{\alpha 1}$ peak is 0.10°, only slightly larger than the value $\Gamma_{2\theta}=0.07°$ obtained for the MgO 002 $K_{\alpha 1}$ substrate peak. This indicates that the CrN(001) layer is of good crystalline quality with no measurable microstrain and negligible variation in lattice parameter. The width Γ_ω of the CrN 002 ω-rocking curve is also relatively narrow, 0.15°, as shown in the inset of Fig. 2(a). Reported Γ_ω values for other epitaxial NaCl structure TM nitrides, 0.6° and 0.9° for TaN(001) and ScN(001),[37,31] respectively, are factors of 4 and 6 larger than that for CrN(001). Thus, the mosaicity of our CrN(001) layers is much lower giving rise to x-ray coherence lengths that are $\simeq 5\times$ larger than for TaN(001) and ScN(001).

Figure 2(b) is a typical HR-RLM about the asymmetric 113 reflection from a 500-nm-thick CrN/MgO(001) layer grown at $T_s=600\,^{\circ}\mathrm{C}$ with $J_{N_2^+}/J_{Cr}=1.7$. Diffracted intensity distributions are plotted as isointensity contours as a function of the reciprocal lattice vectors $k_\parallel$ parallel and $k_\perp$ perpendicular to the surface.[38] For a 113 reflection from an 001-oriented NaCl-structure sample, the in-plane $a_\parallel$ and out-of-plane $a_\perp$ lattice constants are given by $a_\parallel=\sqrt{2}/k_\parallel$ and $a_\perp=3/k_\perp$. Values obtained from the HR-RLM in Fig. 2(b) are 0.4146 and 0.4173 nm, respectively. Thus, the CrN (001) layer is in a state of mild in-plane compressive strain due to differential thermal contraction during cooling from the 600 °C growth temperature. The thermal expansion coefficients for CrN and MgO are $6\times10^{-6}\ K^{-1}$ (Ref. 39) and $1.3\times10^{-5}\ K^{-1}$ (Ref. 40), respectively. Assuming fully relaxed layers during growth and no relaxation during cooling yields an expected CrN in-plane lattice constant of 0.4144 nm, in very good agreement with the measured $a_\parallel$ value of 0.4146 nm.

Parallel and perpendicular lattice constants $a_\parallel$ and $a_\perp$, determined for all epitaxial CrN(001) layers, were found to be $a_\parallel=0.4148\pm0.0007$ nm and $a_\perp=0.4174\pm0.0009$ nm, independent of $J_{N_2^+}/J_{Cr}$ and film growth temperature ($T_s \leqslant 700\,^{\circ}\mathrm{C}$). The relaxed bulk CrN lattice constant a_o is determined from $a_\parallel$ and $a_\perp$ values through the relationship

$$a_o = a_\perp\left(\frac{1-\nu}{1+\nu}\right) + a_\parallel\left(\frac{2\nu}{1+\nu}\right), \tag{1}$$

where $\nu=0.29$ is the Poisson ratio of CrN.[41] We obtain $a_o=0.4162\pm0.0008$ nm, which is within the range of previously reported values, 0.4133–0.4185 nm, obtained from polycrystalline layers and bulk powder samples.[1,19,42–44]

Atomic force microscopy investigations reveal dramatic changes in CrN(001) surface morphology as a function of $J_{N_2^+}/J_{Cr}$. Figure 3 shows typical 3×3 μm^2 AFM images from 500-nm-thick CrN(001) layers grown at $T_s=600\,^{\circ}\mathrm{C}$ with incident ion-to-metal ratios of $J_{N_2^+}/J_{Cr}=1.7$ [Fig. 3(a)] and $J_{N_2^+}/J_{Cr}=14$ [Fig. 3(b)]. The black-to-white gray scales, 14.6 nm in Fig. 3(a) and 7.1 nm in Fig. 3(b), are chosen to be four times the standard deviation of the height distribution around the average value and are therefore proportional to the surface width $\langle w \rangle$ in the corresponding images.

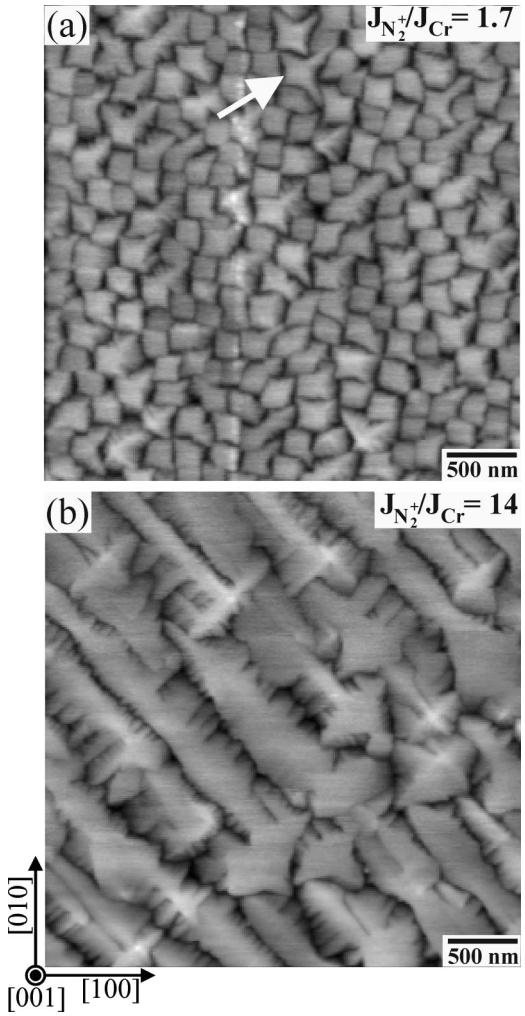

FIG. 3. Atomic force microscopy images (3×3 μm^2 scans) from 500-nm-thick epitaxial CrN/MgO(001) layers grown at $T_s=600\,^{\circ}C$ with (a) $J_{N_2^+}/J_{Cr}=1.7$ and (b) $J_{N_2^+}/J_{Cr}=14$. The black-to-white scale corresponds to 14.6 and 7.1 nm for (a) and (b), respectively.

The surface morphology of the CrN(001) layer grown with $J_{N_2^+}/J_{Cr}=1.7$ [Fig. 3(a)], which corresponds to typical conditions for standard magnetron sputter deposition systems, exhibits primarily square growth mounds with edges predominantly aligned along low-energy ⟨100⟩ directions.[45] Lateral mound sizes range from 130 to 300 nm with a surface width $\langle w\rangle$, obtained from the height-difference correlation function, of 1.80 ± 0.04 nm. The latter yields an average peak-to-valley mound height $\langle h\rangle=5.09\pm0.11$ nm. The in-plane correlation length $\langle d\rangle$ is 208 ± 20 nm. Thus, the mound aspect ratio $\langle h\rangle/\langle d\rangle$ is 0.024.

Some mounds in Fig. 3(a) (see example marked with white arrow) have corners elongated along ⟨110⟩ directions. We attribute the formation of these mounds, which have the shape of a distorted four-cornered star, to the incorporation of small mounds into larger ones through coalescence at adjacent corners along ⟨110⟩ directions. Preferential corner coalescence, which begins to occur, as discussed below, at layer thicknesses of ≃30 nm, can be explained as follows. Growth mounds form due to kinetic surface roughening during deposition under conditions of low adatom mobility in the presence of Ehrlich barriers to adatom migration over descending step edges.[46] Mound formation is exacerbated during sputter deposition due to the large component of non-normal deposition flux,[47] which results in atomic shadowing and, hence, a decrease in the flux reaching the valleys between the mounds. Shadowing is strongest along ⟨100⟩ valleys and less pronounced at corners. Consequently, ⟨100⟩-oriented valleys are deeper than the dips between mound corners along the ⟨110⟩ directions. This, in turn, favors coalescence along the ⟨110⟩ directions.

The AFM image in Fig. 3(b) is obtained from a CrN(001) layer grown with a high ion-to-metal flux ratio, $J_{N_2^+}/J_{Cr}=14$. The surface of this sample exhibits a strikingly different morphology than that shown in Fig. 3(a) which is characteristic of sputter deposition under low ion-to-metal flux ratios. The growth mounds in Fig. 3(b) are much larger and elongated along ⟨110⟩ while dendritic in the orthogonal direction. Analysis of a 100 μm^2 area scan shows that the average length-to-width ratio is 4 ± 1. Although the mounds in Fig. 3(b) tend to be elongated along $[1\bar{1}0]$, with dendritic edges exhibiting arms along [110], larger area images indicate that there is an equal probability for islands to be elongated along [110] as expected from the underlying cubic symmetry. Thus, the surface exhibits a two-domain structure with the domain boundary corresponding to a 90° rotation in the mound elongation direction. The overall ⟨110⟩-directionality is again attributed to preferential mound corner coalescence.

The in plane areas A of growth mounds on CrN(001) layers deposited with $J_{N_2^+}/J_{Cr}=14$ range from 0.25 to 1.5 μm^2, approximately an order of magnitude larger than A values from samples grown with $J_{N_2^+}/J_{Cr}=1.7$ [Fig. 3(a)]. In addition, the average mound height, $\langle h\rangle=2.52\pm0.03$ nm, decreases by $\simeq2\times$ while the in-plane correlation length, $\langle d\rangle=520\pm100$ nm,[48] is $2.5\times$ larger. This results in an average aspect ratio $\langle h\rangle/\langle d\rangle=0.005$ for the CrN(001) layer grown with $J_{N_2^+}/J_{Cr}=14$, a factor of 5 lower than that obtained for the $J_{N_2^+}/J_{Cr}=1.7$ CrN(001) layer.

The above results show that increasing the incident ion-to-metal flux ratio, at low N_2^+ ion energies, during the growth of CrN(001) results in smoother surfaces with both smaller mound heights and decreased mound aspect ratios. High-flux, low-energy, ion irradiation leads to higher adatom mean surface diffusion lengths and, consequently, larger surface features. Similar trends have been observed for the low-temperature growth of Si/Si(001) and $Si_{1-x}Ge_x$/Si(001) from hyperthermal (15–18 eV) beams in which not only smoother surfaces, but also larger critical epitaxial thicknesses were obtained.[49,50] Microstructural changes attributed to N_2^+-ion-irradiation induced enhancements in adatom mobilities have also been reported for other TM nitrides including TiN,[30] $Ti_{0.5}Al_{0.5}N$,[31] and ScN.[32] In addition to larger adatom diffusion lengths on terraces, momentum transfer from low-energy ion irradiation increases the probability of adatoms crossing descending step edges. This contributes to the filling of trenches between growth mounds, thereby reducing atomic shadowing. The surface smoothening obtained at higher ion-to-metal flux ratios also has important conse-

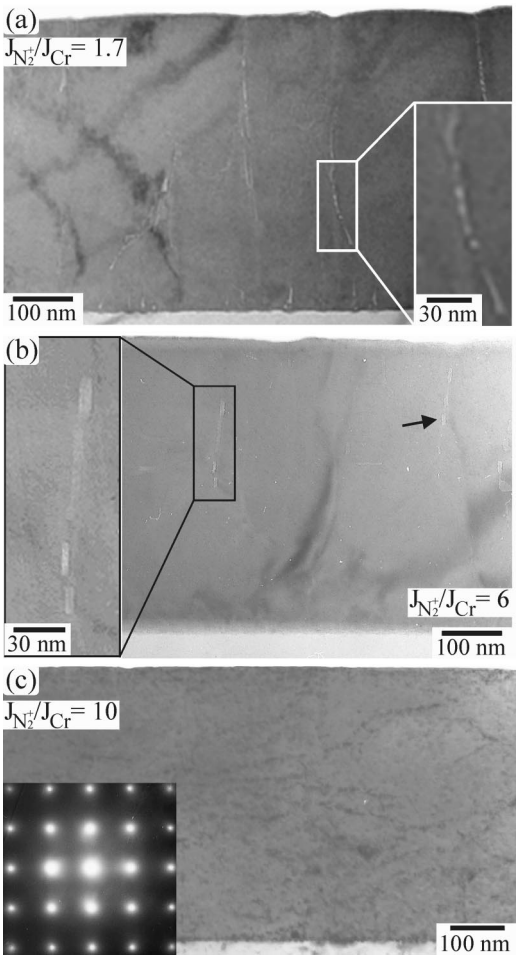

FIG. 4. XTEM micrographs from 500-nm-thick epitaxial CrN/MgO(001) layers grown at $T_s = 600\,^{\circ}\mathrm{C}$ with (a) $J_{N_2^+}/J_{Cr} = 1.7$, (b) $J_{N_2^+}/J_{Cr} = 6$, and (c) $J_{N_2^+}/J_{Cr} = 10$. The inserts in (a) and (b) show higher resolution images of typical nanopipes while the inset in (c) is a corresponding SAED pattern.

quences for bulk CrN(001) microstructural evolution as illustrated by the XTEM results discussed below.

While high-flux, low-energy, ion irradiation enhances adatom mobilities on terraces, the increasingly dendritic mound shape obtained with higher $J_{N_2^+}/J_{Cr}$ values, as illustrated in Fig. 3(b), suggests that N_2^+ irradiation actually decreases adatom mobilities along step edges giving rise to two-dimensional (2D) atomic shadowing. We attribute the ''hit and stick'' behavior at step edges to a secondary ion/surface interaction effect. The large N_2^+ flux incident at the growth surface gives rise to a higher steady-state atomic N surface population due to collisionally induced dissociative chemisorption. The excess atomic N diffuses on the surface and attaches at step edges, leading to N-oversaturated step edges which decrease cation edge mobilities.

Figure 4 shows typical XTEM images from 500-nm-thick epitaxial CrN/MgO(001) layers grown at $T_s = 600\,^{\circ}\mathrm{C}$ with $J_{N_2^+}/J_{Cr} = 1.7$, 6, and 10. The 100 zone axis cross-sectional selected area electron diffraction (SAED) pattern in Fig. 4(c) from the sample grown with $J_{N_2^+}/J_{Cr} = 10$ is essentially identical to results obtained from all stoichiometric films, irrespective of T_s and $J_{N_2^+}/J_{Cr}$. The SAED pattern exhibits symmetric single-crystal reflections revealing a cube-on-cube epitaxial relationship: $(001)_{CrN}||(001)_{MgO}$ with $[100]_{CrN}||[100]_{MgO}$.

An XTEM micrograph from a CrN(001) layer grown with $J_{N_2^+}/J_{Cr} = 1.7$ is presented in Fig. 4(a). The image, obtained close to the 100 zone axis, shows that the film/substrate interface is abrupt, with misfit dislocations visible due to strain field contrast. The most prominent features in this layer are 1–5 nm wide nanopipes along the [001] growth direction. A higher-resolution image of a short section of a typical nanopipe is shown in the inset in Fig. 4(a). The nanopipes are underdense regions which appear bright when the image is underfocused, as is the case for all micrographs in Fig. 4, but appear dark when viewed in overfocused conditions.

The XTEM image in Fig. 4(a) reveals 10 nanopipes in the field of view, all originating from the CrN/MgO(001) interface. The average lateral separation $\langle s \rangle$ between nanopipes is 90 ± 20 nm. At film thickness $t \simeq 30$ nm, corresponding to the onset of mound coalescence, half of the nanopipes terminate. That is, the nanopipe density decreases by a factor of 2 while $\langle s \rangle$ increases to 180 ± 40 nm, approximately equal to the growth mound in-plane correlation length $\langle d \rangle = 208 \pm 20$ nm, determined from the AFM image of this sample in Fig. 3(a). The remaining five nanopipes continue to the free surface where they terminate at cusps between growth mounds. The nanopipe density, determined from large area plan-view TEM micrographs, was found to be $\simeq 870\ \mu\mathrm{m}^{-2}$. This number is larger than the surface mound density, $48\ \mu\mathrm{m}^{-2}$, since each valley between adjacent mounds contains several nanopipes. The combination of low- and high-resolution XTEM images shows that the surface exhibits a periodic mound structure with an average mound height $\langle h \rangle \simeq 5$ nm and a mound-to-mound spacing of 220 ± 70 nm, in good agreement with the AFM results.

Our TEM investigations suggest that the formation of nanopipes is directly related to the presence of the surface cusps between the periodic growth mounds. The overall surface morphology is characteristic of kinetic roughening previously observed in cubic semiconductor,[49,51–54] metal,[55] and TM nitride[56,57] films grown at relatively low homologous temperatures. The mounds are aligned along low-energy $\langle 100 \rangle$, step edge directions (i.e., along nonpolar Cr–N bonding directions) with the development of deep cusps. The local deposition rate at the bottom of the cusps is reduced due to atomic shadowing which, in combination with limited adatom mobility, gives rise to the formation of nanopipes similar to those previously observed in ScN(001) and TaN(001) layers deposited on MgO(001) by reactive sputtering.[31,58,59]

The XTEM micrograph in Fig. 4(b) was obtained from a CrN(001) layer grown with $J_{N_2^+}/J_{Cr} = 6$. The layer appears defect-free (no nanopipes) over a layer thickness $t^* \simeq 250$ nm with a low nanopipe density at $t > t^*$. Two nanopipes are observed in the field of view in Fig. 4(b); one is shown at higher magnification while the other is indicated by a black arrow. The nanopipe density determined from low-magnification plan-view micrographs is $\simeq 270\ \mu\mathrm{m}^{-2}$, more

than a factor of 3 less than in CrN(001) layers grown with $J_{N_2^+}/J_{Cr}=1.7$. The nanopipes, as was the case for the layer grown at the low ion-to-metal ratio, have widths ranging from 1 to 5 nm. However, they are not continuous and appear and disappear along the growth direction (see higher resolution view). While the nanopipe on the left-hand side of Fig. 4(b) terminates well below the surface, the nanopipe on the right reaches the surface at a cusp between two mounds. The average mound-to-mound spacing determined from XTEM is 280 ± 80 nm and the mound height $\simeq 4$ nm. Thus, as $J_{N_2^+}/J_{Cr}$ is increased from 1.7 to 6, the in-plane mound size increases while the height decreases, in agreement with the results of our AFM investigations.

Figure 4(c) is a typical XTEM micrograph from a CrN(001) sample grown with $J_{N_2^+}/J_{Cr}=10$. The surface appears flat to within the resolution of the microscope, consistent with our AFM images which show very low surface roughness aspect ratios for CrN(001) layers grown with $J_{N_2^+}/J_{Cr}\geqslant 10$. No nanopipes are observed in Fig. 4(c). A detailed analysis of multiple XTEM images from many layers grown with $J_{N_2^+}/J_{Cr}=10$ and 14 reveals, however, the presence of nanopipes above a film thickness $t^*\simeq 400$ nm, but with a very low number density. Large-area plan-view micrographs provide an upper limit of 20 μm^{-2} for the nanopipe number density in these layers, more than 40 times less than for CrN(001) layers grown with $J_{N_2^+}/J_{Cr}=1.7$.

Thus, the strong effects of low-energy N_2^+ ion irradiation during deposition on the surface morphology of CrN(001) layers, as discussed above, also controls the formation rate of nanopipes. Layers grown with low ion-to-metal ratios ($J_{N_2^+}/J_{Cr}=1.7$) exhibit rough surfaces composed of growth mounds with relatively high aspect ratios, 0.024, and short in-plane coherence lengths, $\langle d\rangle=208$ nm, which, within the experimental uncertainty, are equal to the measured average separations between nanopipes. The higher nanopipe density observed at $t<30$ nm for layers grown with $J_{N_2^+}/J_{Cr}=1.7$ results from the fact that mound sizes are smaller ($\simeq$90 nm) during the initial stages of CrN(001) growth prior to mound coalescence.

For CrN(001) layers grown with medium ion-to-metal ratios, $J_{N_2^+}/J_{Cr}=6$, the in-plane correlation length is larger, corresponding to a lower mound number density. This, in turn, results in a reduction in the nanopipe number density by more than a factor of 3 compared to CrN(001) layers grown with $J_{N_2^+}/J_{Cr}=1.7$. In addition, nanopipes form only above a critical film thickness ($t^*\simeq 250$ nm) and are found to be discontinuous along the growth direction. The rate of surface roughening occurs more gradually during growth with $J_{N_2^+}/J_{Cr}=6$. Thus, at $t<t^*$, the mound aspect ratio is too small to provide sufficient atomic shadowing to form cusps and, hence, nanopipes. Even at $t>t^*$, the surface roughness is not adequate to sustain continuous nanopipe formation, leading to discontinuous nanopipes. At high ion-to-metal flux ratios, $J_{N_2^+}/J_{Cr}\geqslant 10$, layer surfaces are relatively smooth, $\langle w\rangle=0.89$ nm, such that shadowing is negligible and essentially no nanopipes are formed.

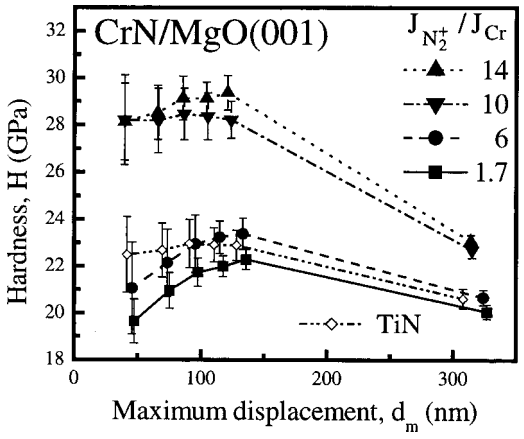

FIG. 5. Measured hardness values as a function of maximum displacement d_m obtained from nanoindentation measurements on 0.5-μm-thick epitaxial CrN/MgO(001) layers grown at $T_s=600\,^\circ$C with $J_{N_2^+}/J_{Cr}=1.7$, 6, 10, and 14. H vs d_m values are also given for an epitaxial TiN/MgO(001) reference sample.

D. Resistivity and mechanical properties

The room-temperature resistivity ρ of epitaxial CrN(001) layers grown at $T_s=600\,^\circ$C is $(7.7\pm0.5)\times10^{-2}\ \Omega$ cm, independent of $J_{N_2^+}/J_{Cr}$. This is within the range of previously reported values, 3×10^{-4} to $6\times10^{2}\ \Omega$ cm, obtained from polycrystalline CrN_x powders and thin films.[15–18] The wide variation in published resistivities for polycrystalline CrN is due to large, and primarily uncharacterized, differences in stoichiometry and/or microstructure including grain size, porosity, and defect concentration.

The hardnesses H and elastic moduli E of our CrN(001) layers were determined from nanoindentation measurements using a three-sided pyramidal Berkovich diamond indentor tip following the technique developed in Ref. 28. Figure 5 shows measured hardness values as a function of maximum displacement d_m, i.e., indentation depth, for 0.5-μm-thick epitaxial CrN(001) layers grown at 600 °C with $J_{N_2^+}/J_{Cr}=1.7$, 6, 10, and 14. The data plotted in Fig. 5 represent average values from more than 25 indentation sequences per data point and are obtained from unloading curves with maximum loads of 2, 4, 6, 8, 10, and 40 mN. For comparison, the measured hardnesses as a function of displacement are also plotted for a 0.5-μm-thick fully dense epitaxial TiN(001)/MgO(001) reference layer grown in pure N_2 at 800 °C. H, at $d_m\leqslant 150$ nm, was found to be 23 ± 2 GPa, in reasonable agreement with the previously reported value, 20 ± 0.8 GPa, for epitaxial TiN(001) grown at 700 °C in an $Ar+N_2$ gas mixture.[28]

The CrN(001) layer deposited with $J_{N_2^+}/J_{Cr}=1.7$ has a near-surface ($d_m=50$ nm) hardness of 20 GPa. H then increases with increasing indentation depths to 22 GPa at 100 nm $\leqslant d_m\leqslant 150$ nm and subsequently decreases with $d_m>150$ nm. The data from $J_{N_2^+}/J_{Cr}=6$ layers exhibit a similar trend with, however, slightly higher hardness values; 21 GPa at small indentation depths and 23 GPa at 100 nm $\leqslant d_m\leqslant 150$ nm. In distinct contrast, layers grown with $J_{N_2^+}/J_{Cr}=10$ and 14 exhibit much higher hardness values, 28.5 ± 1

GPa, which are essentially independent of $d_m < 150$ nm.

We attribute the increase in hardness with increasing d_m for CrN(001) layers grown with low ion-to-metal ratios ($J_{N_2^+}/J_{Cr} = 1.7$) to their lower density, due to the presence of nanopipes, reducing the resistance to indentation loads. Thus, measured hardnesses for these layers are lower at small indentation depths where a significant fraction of the plastic deformation corresponds to densification of nanopipes. At intermediate loads, ranging from 6 to 10 mN ($d_m = 100-150$ nm), the measured hardness values exhibit less variation indicating that bulk plastic deformation at $d_m \geqslant 100$ nm is considerably larger than the contribution due to nanopipe densification, rendering the latter negligible. However, bulk plastic deformation is enhanced, as noted below, by the presence of nanopipes, even when they are densified, since such structural defects act as sources and sinks for dislocations. The decrease in H for maximum displacements larger than 150 nm, corresponding to 30% of the layer thickness, is due to substrate effects. MgO(001), with a hardness of only 9 GPa,[28] is much softer than CrN(001). Similar H vs d_m results are obtained for CrN(001) layers grown with $J_{N_2^+}/J_{Cr} = 6$ except that the overall curve is shifted to higher H values due to the presence of fewer nanopipes.

Increasing $J_{N_2^+}/J_{Cr} \geqslant 10$, yielding CrN(001) layers with few or no nanopipes, results in much higher H values with $H(d_m)$ curves which remain nearly constant at $d_m < 150$ nm, since the densification, described above, is absent for layers with essentially no nanopipes. The much higher H values for layers grown with $J_{N_2^+}/J_{Cr} \geqslant 10$ shows that the presence of nanopipes dramatically reduces H. This is likely due to nanopipes acting as nucleation sites for dislocation formation. The intrinsic hardness of dense CrN(001) is $\simeq 28.5$ GPa.

The elastic modulus E of our CrN(001) samples was also determined from the nanoindentation experiments and found to be 405 ± 15 GPa for all samples, independent of $J_{N_2^+}/J_{Cr}$. Thus, E is unaffected by the presence of nanopipes. This is as expected since E, in contrast to H, is a purely elastic property and the total volume fraction occupied by nanopipes is always less than 2%, even with $J_{N_2^+}/J_{Cr} = 1.7$.

The fact that a_o, E, and ρ are all independent of $J_{N_2^+}/J_{Cr}$, indicates that high-flux, low-energy N_2^+ ion irradiation during CrN(001) growth does not lead to significant residual point defect concentrations since this would give rise to measurable changes in these properties as a function of $J_{N_2^+}/J_{Cr}$. Thus, $a_o = 0.4162 \pm 0.0008$ nm, $\rho = 7.7 \times 10^{-2}$ Ω cm, $E = 405 \pm 15$ GPa, and $H = 28.5 \pm 1$ GPa correspond to intrinsic fundamental properties for NaCl-structure CrN(001).

IV. CONCLUSIONS

CrN layers grown on MgO(001) by reactive magnetically unbalanced ultrahigh vacuum magnetron sputtering in pure N_2 discharges at 20 mTorr have the NaCl structure and are stoichiometric, with N/Cr ratios $= 1.00 \pm 0.03$ for deposition temperatures $570 \leqslant T_s \leqslant 700$ °C. However, at higher growth temperatures, N_2 desorption during deposition results in understoichiometric layers with N-fraction f_N decreasing to 0.35, 0.28, and 0.07 at $T_s = 730$, 760, and 775 °C. The high-temperature samples are multiphase polycrystalline films containing mixtures of NaCl-structure CrN_x, hexagonal β-Cr_2N, and bcc-Cr. In contrast, CrN layers grown at $T_s \leqslant 700$ °C are stoichiometric single crystals exhibiting a cube-on-cube epitaxial relationship with the substrate, $(001)_{CrN} || (001)_{MgO}$ with $[100]_{CrN} || [100]_{MgO}$, and a relaxed lattice constant $a_o = 0.4162 \pm 0.0008$ nm.

Deposition in the magnetically balanced mode with no external magnetic field ($B_{ext} = 0$), typical of standard magnetron sputtering conditions, results in a N_2^+-ion to Cr-atom flux ratio incident at the growing film surface of $J_{N_2^+}/J_{Cr} = 1.7$. Growth under these condition leads to a CrN(001) surface morphology which exhibits kinetic roughening with the development of self-organized square-shaped surface mounds with edges aligned along orthogonal ⟨100⟩ directions. The mounds have an average peak-to-valley height $\langle h \rangle = 5.1$ nm and an in-plane correlation length of $\langle d \rangle = 0.21$ μm corresponding to a height-to-width aspect ratio of 0.024. The rough growth surface together with the large angular distribution of the deposition flux, inherent to sputter deposition, leads to 3D atomic shadowing. This, in turn, results, under low adatom mobility conditions, to the formation of deep cusps and 1–5 nm wide nanopipes which are elongated along the growth direction and terminate at the surface. The average nanopipe separation, 180 ± 40 nm, is, within the experimental uncertainty, equal to the in-plane surface mound coherence length.

Applying an external magnetic field $B_{ext} = 60$, 120, and 180 G during deposition increases the ion-to-metal flux ratio $J_{N_2^+}/J_{Cr}$ to 6, 10, and 14, respectively, while the N_2^+-ion energy remains constant at 12 eV. The increase in N_2^+-flux leads to enhanced adatom surface diffusion which, in turn, results in dramatic changes in surface morphological evolution. The surfaces of CrN(001) layers grown with $J_{N_2^+}/J_{Cr} = 14$ exhibit growth mounds which are elongated along ⟨110⟩ and dendritic in the perpendicular direction. Their average height $\langle h \rangle = 2.5$ nm is 2× smaller and the in-plane correlation length $\langle d \rangle = 0.52$ μm is 2.5× larger than obtained with $J_{N_2^+}/J_{Cr} = 1.7$. Thus, surfaces grown with high $J_{N_2^+}/J_{Cr}$ are much smoother, with 5× smaller mound aspect ratios, leading to a decreased amount of atomic shadowing and consequently a lower nanopipe number density, determined to be 870, 270, and < 20 μm^{-2} with $J_{N_2^+}/J_{Cr} = 1.7$, 6, and 10, respectively.

Measured CrN(001) hardness values depend strongly on the presence of nanopipes. $H = 28.5 \pm 1$ GPa for layers grown with $J_{N_2^+}/J_{Cr} \geqslant 10$ and containing essentially no nanopipes. However, H decreases to 22.5 ± 1 GPa for layers exhibiting significant nanopipe number densities ($\geqslant 270$ μm^{-2}, $J_{N_2^+}/J_{Cr} \leqslant 6$), suggesting that nanopipes can act as centers for dislocation formation.

The elastic modulus and room-temperature resistivity of CrN(001) are independent of $J_{N_2^+}/J_{Cr}$, indicating that 12 eV N_2^+-ion irradiation during film growth does not produce significant concentrations of point defects. Thus, $a_o = 0.4162 \pm 0.0008$ nm, $\rho = 7.7 \times 10^{-2}$ Ω cm, $E = 405 \pm 15$ GPa, and

$H = 28.5 \pm 1$ GPa correspond to intrinsic fundamental properties for NaCl-structure CrN(001).

ACKNOWLEDGMENTS

This work was supported by the U.S. Department of Energy, Division of Materials Science, under Grant No. DEFG02-96ER45439 through the University of Illinois Frederick Seitz Materials Research Laboratory (MRL) and the Division of Materials Research, National Science Foundation. We also appreciate the use of the facilities of the MRL Center for Microanalysis of Materials, which is partially supported by DOE, at the University of Illinois, and thank M. Sardela and Y. W. Kim for assistance with XRD and TEM analyses. C.S.S. was partially supported by Hynix Semiconductor Inc. in Korea.

[1] P. Hones, M. Diserens, R. Sanjinés, and F. Lévy, J. Vac. Sci. Technol. B **18**, 2851 (2000).
[2] P. Hones, C. Zakri, P. E. Schmid, F. Lévy, and O. R. Shojaei, Appl. Phys. Lett. **76**, 3194 (2000).
[3] I. Milosev, J. M. Abels, H.-H. Strehblow, B. Navinsek, and M. Metikos-Hukovic, J. Vac. Sci. Technol. A **14**, 2527 (1996).
[4] J. Stockemer, R. Winand, and P. V. Brande, Surf. Coat. Technol. **115**, 230 (1999).
[5] C. P. Constable, J. Yarwood, P. Hovsepian, L. A. Donohue, D. B. Lewis, and W.-D. Münz, J. Vac. Sci. Technol. A **18**, 1681 (2000).
[6] L. Cunha, M. Andritschky, L. Rebouta, and K. Pischow, Surf. Coat. Technol. **116**, 1152 (1999).
[7] A. Fayer, O. Glozman, and A. Hoffman, Appl. Phys. Lett. **67**, 2299 (1995).
[8] P. F. Carcia, R. H. French, M. H. Reilly, M. F. Lemon, and D. J. Jones, Appl. Phys. Lett. **70**, 2371 (1997).
[9] S. Tsuboi, S. Kotsuji, T. Yoshihara, and K. Suzuki, J. Vac. Sci. Technol. B **15**, 2228 (1997).
[10] M. Odén, C. Ericsson, G. Hakansson, and H. Ljungcrantz, Surf. Coat. Technol. **114**, 39 (1999).
[11] X.-M. He, N. Baker, B. A. Kehler, K. C. Walter, and M. Nastasi, J. Vac. Sci. Technol. A **18**, 30 (2000).
[12] T. Hurkmans, D. B. Lewis, H. Paritong, J. S. Brooks, and W. D. Münz, Surf. Coat. Technol. **114**, 52 (1999).
[13] T. Nyberg, P. Skytt, B. Galnander, C. Nender, J. Nordgren, and S. Berg, J. Vac. Sci. Technol. A **15**, 248 (1997).
[14] J. Almer, M. Odén, L. Hultman, and G. Hakansson, J. Vac. Sci. Technol. A **18**, 121 (2000).
[15] P. Panjan, B. Navisek, A. Cvelbar, A. Zalar, and J. Vlcek, Surf. Coat. Technol. **98**, 1497 (1998).
[16] R. Mientus and K. Ellmer, Surf. Coat. Technol. **116–119**, 1093 (1999).
[17] P. S. Herle, M. S. Hegde, N. Y. Vastahacharya, S. Philip, M. V. R. Rao, and T. Sripathi, J. Solid State Chem. **134**, 120 (1997).
[18] Y. Tsuchiya, K. Kosuge, Y. Ikeda, T. Shigematsu, S. Yamaguchi, and N. Nakayama, Mater. Trans., JIM **37**, 121 (1996).
[19] H. Hasegawa, A. Kimura, and T. Suzuki, J. Vac. Sci. Technol. A **18**, 1038 (2000).
[20] M. L. Kuruppu, G. Negrea, I. P. Ivanov, and S. L. Rohde, J. Vac. Sci. Technol. A **16**, 1949 (1998).
[21] F. Esaka, K. Furuya, H. Shimada, M. Imamura, N. Matsubayashi, H. Sato, A. Nishijima, A. Kawana, H. Ichimura, and T. Kikuchi, J. Vac. Sci. Technol. A **15**, 2521 (1997).
[22] P. Yashar, X. Chu, S. A. Barnett, J. Rechner, Y. Y. Wang, M. S. Wong, and W. D. Sproul, Appl. Phys. Lett. **72**, 9987 (1998).
[23] The CrN bulk-atom displacement energy is expected to be between 20 and 50 eV, based on reports from other NaCl-structure TM nitrides, ScN and $Ti_{0.5}Al_{0.5}N$ in Refs. 31 and 32. The latter materials exhibit no bulk displacement under $E_i = 20$ eV N_2^+ irradiation but ion-induced defects are detectable with $E_i = 50$ eV.
[24] I. Petrov, F. Adibi, J. E. Greene, W. D. Sproul, and W.-D. Münz, J. Vac. Sci. Technol. A **10**, 3283 (1992).
[25] R. C. Powell, N.-E. Lee, Y.-W. Kim, and J. E. Greene, J. Appl. Phys. **73**, 189 (1998).
[26] L. R. Doolittle, Nucl. Instrum. Methods Phys. Res. B **9**, 344 (1985).
[27] W. C. Oliver and G. M. Pharr, J. Mater. Res. **7**, 1564 (1992).
[28] H. Ljungcrantz, M. Odén, L. Hultman, J. E. Greene, and J.-E. Sundgren, J. Appl. Phys. **80**, 6725 (1996).
[29] I. Petrov, A. Myers, J. E. Greene, and J. R. Abelson, J. Vac. Sci. Technol. A **12**, 2846 (1994).
[30] J. E. Greene, J.-E. Sundgren, L. Hultman, I. Petrov, and D. B. Bergstrom, Appl. Phys. Lett. **67**, 2928 (1995).
[31] D. Gall, I. Petrov, N. Hellgren, L. Hultman, J.-E. Sundgren, and J. E. Greene, J. Appl. Phys. **84**, 6034 (1998).
[32] F. Adibi, I. Petrov, J. E. Greene, L. Hultman, and J. E. Sundgren, J. Appl. Phys. **73**, 8580 (1993).
[33] A. V. Phelps, J. Phys. Chem. Ref. Data **20**, 557 (1991).
[34] B. Chapman, *Glow Discharge Processes* (Wiley, New York, 1980), p. 108.
[35] H. F. Winters, J. Chem. Phys. **43**, 926 (1965); **44**, 1472 (1966).
[36] H. Kimura, I. Petrov, F. Adibi, and J. E. Greene, J. Cryst. Growth **123**, 344 (1992).
[37] C.-S. Shin, D. Gall, P. Desjardins, A. Vailionis, H. Kim, I. Petrov, J. E. Greene, and M. Odén, Appl. Phys. Lett. **75**, 3808 (1999).
[38] P. van der Sluis, J. Phys. D **26**, A188 (1993).
[39] M. Eddine, F. Sayetat, and E. F. Bertaut, C. R. Hebd. Seances Acad. Sci., Ser. B **269**, 574 (1969).
[40] H. Landolt and R. Börnstein, *Numerical Data and Functional Relationships in Science and Technology, Group III* (Springer, Berlin, 1975), Vol. 7, Part. B1, p. 27.
[41] U. Wiklund, M. Bromark, M. Larsson, P. Hedenqvist, and S. Hogmark, Surf. Coat. Technol. **91**, 57 (1997).
[42] JCPDS File Card No. 11-0065.
[43] P. M. Fabis, R. A. Cooke, and S. McDonough, J. Vac. Sci. Technol. A **8**, 3819 (1990).
[44] L. Cuhha and M. Andritschky, Surf. Coat. Technol. **111**, 158 (1999).
[45] ⟨100⟩-step edges are, in analogy to nonpolar {100} surfaces, expected to be the low-energy orientation since they are parallel to the Cr–N bond direction in NaCl-structure CrN.
[46] S. C. Wang and G. Ehrlich, Phys. Rev. Lett. **70**, 41 (1993); **71**, 4177 (1993); G. Ehrlich, Surf. Sci. **331/333**, 865 (1995); A. Gölzhäuser and G. Ehrlich, Phys. Rev. Lett. **77**, 1334 (1996).
[47] Sputter deposition typically results in a cosine distribution of the incoming atom flux with the highest flux at an azimuthal angle of 45°. H. Huang, G. H. Gilmer, and T. D. de la Rubia, J. Appl. Phys. **84**, 3636 (1998).
[48] The relatively large uncertainty stems from the fact that $\langle d \rangle$ was obtained from a height–height correlation function which assumes isotropic surface morphology.
[49] N.-E. Lee, G. Xue, and J. E. Greene, J. Appl. Phys. **80**, 769 (1996).
[50] N.-E. Lee, M. Matsuoka, M. R. Sardela, F. Tian, and J. E. Greene, J. Appl. Phys. **80**, 812 (1996).
[51] N.-E. Lee, D. G. Cahill, and J. E. Greene, J. Appl. Phys. **80**, 2199 (1996).
[52] G. Xue, H. Z. Xiao, M.-A. Hasan, J. E. Greene, and H. K. Birnbaum, J. Appl. Phys. **74**, 2512 (1993).
[53] N.-E. Lee, G. A. Tomasch, and J. E. Greene, Appl. Phys. Lett. **65**, 3236 (1994).
[54] D. J. Eaglesham, H.-J. Gossmann, and M. Cerullo, Phys. Rev. Lett. **65**, 1227 (1990).
[55] J. A. Stroscio, D. T. Piercee, M. D. Stiles, A. Zangwill, and L. M. Sander, Phys. Rev. Lett. **75**, 4246 (1995).
[56] B. W. Karr, I. Petrov, D. G. Cahill, and J. E. Greene, Appl. Phys. Lett. **70**, 1703 (1997).
[57] B. W. Karr, I. Petrov, P. Desjardins, D. G. Cahill, and J. E. Greene, Surf. Coat. Technol. **94/95**, 403 (1997).
[58] D. Gall, I. Petrov, P. Desjardins, and J. E. Greene, J. Appl. Phys. **86**, 5524 (1999).
[59] C.-S. Shin, Y.-W. Kim, D. Gall, J. E. Greene, and I. Petrov (unpublished).